




# Electrostatic Dust Analyzer for Dust Transport Measurements on the Lunar Surface

X. Wang<sup>1,2</sup> , M. Horanyi<sup>1,2</sup>, C. Fisher<sup>2</sup>, L. Eberwein<sup>1,2</sup>, J. Deca<sup>1,2</sup>, S. Knappmiller<sup>2</sup>, D. Hansen<sup>2</sup>, Z. Levin<sup>1,2</sup>, R. Wing<sup>2</sup>, D. Summers<sup>2</sup>, W. Cole<sup>2</sup>, P. Buedel<sup>2</sup>, J. Drouet<sup>2</sup>, S. Tucker<sup>2</sup>, and I. Garrick-Bethell<sup>3</sup>

<sup>1</sup> NASA SSERVI's Institute for Modeling Plasma, Atmospheres, and Cosmic Dust (IMPACT), University of Colorado Boulder, Boulder, CO 80303, USA

<sup>2</sup> Laboratory for Atmospheric and Space Physics (LASP), University of Colorado Boulder, Boulder, CO 80303, USA

<sup>3</sup> Department of Earth & Planetary Sciences, University of California, Santa Cruz, CA 95064, USA

Received 2023 December 12; revised 2024 January 15; accepted 2024 January 15; published 2024 February 20

## Abstract

Lunar dust charging and transport is a more than five-decade-old problem. A high-fidelity and flight-qualified Electrostatic Dust Analyzer (EDA) has been developed to measure the charge, velocity, mass (size), and flux of electrostatically lofted dust particles on the lunar surface. Recent laboratory findings have greatly advanced our fundamental understanding of the dust-charging and -lofting mechanisms, providing critical constraints to the design of the EDA instrument. EDA consists of two identical dust trajectory sensor (DTS) units on both ends of the instrument with a deflection field electrode (DFE) unit lying in between. When a dust particle enters the instrument, charge signals induced on four arrays of wire electrodes in the two DTS units determine the total charge of the dust particle and its trajectory passing through the instrument from which the dust velocity vector is measured. The mass (size) is derived from the deflection of the dust trajectory by the DFE. A dust campaign was performed to characterize the instrument's performance. The results meet or exceed the requirements. EDA has achieved high Technology Readiness Level 6. EDA measurements are important for assessing the dust environment on the lunar surface and its subsequent impact on crew safety and the operation of exploration systems. Additionally, EDA measurements are expected to have important implications for the surface evolution of all airless bodies, including the Moon and asteroids, in the solar system.

*Unified Astronomy Thesaurus concepts:* [The Moon \(1692\)](#); [Lunar science \(972\)](#); [Dust physics \(2229\)](#); [Plasma physics \(2089\)](#); [Space plasmas \(1544\)](#)

## 1. Introduction

The lunar surface is directly exposed to the solar wind plasma and solar ultraviolet (UV) radiation, resulting in charging of dust particles on the surface. It has been hypothesized that charged dust particles may be mobilized, lofted, and transported due to electrostatic forces. The first evidence suggesting electrostatic dust transport was the Lunar Horizon Glow (LHG) observed shortly after sunset by the Surveyor 5, 6, and 7 landers in late 1960s. The bright glow,  $\sim 30$  cm above the lunar surface, was believed to be sunlight scattered off a cloud of dust particles ( $\sim 5 \mu\text{m}$  in radii) electrostatically lofted or levitated (Criswell 1973; Rennilson & Criswell 1974). Interestingly, the height of the LHG is consistent with recent observations by the Chang'e-3 rover of fine dust deposits on lunar rocks up to 28 cm high (Yan et al. 2019).

Several Apollo observations also indicated the occurrence of electrostatic dust transport. The Lunar Ejecta and Meteorites Experiment (LEAM) deployed on the lunar surface registered low-speed ( $< 100 \text{ m s}^{-1}$ ) dust particles with the rate spiking at both sunrise and sunset (Berg et al. 1976), which was suggested to be caused by the transient enhancement of electric fields across the lunar terminator. However, later work by Grün & Horányi (2013), after revisiting different LEAM data sets, found no significant rate enhancement associated with terminator crossings. High-altitude streamers observed by Apollo 17 astronauts in lunar orbit were also suggested to be due to nanometer-sized dust particles electrostatically lofted to 10–100 km altitudes (McCoy & Criswell 1974; Zook &

McCoy 1991). Apollo images from orbit also indicated an excess brightness over the zodiacal light (McCoy 1976; Glenar et al. 2011). However, such a dense dust population was neither confirmed by later remote-sensing observations by Clementine (Glenar et al. 2014) and the Lunar Reconnaissance Orbiter/Lyman Alpha Mapping Project (LRO/LAMP; Feldman et al. 2014) nor indicated from in situ measurements by the Lunar Atmosphere and Dust Environment Explorer/Lunar Dust Experiment (LADEE/LDEX; Szalay & Horányi 2015). As unique features colocated with strong lunar magnetic anomalies, high-albedo lunar swirls have attracted much interest in understanding their formation (Blewett et al. 2011). One of the hypotheses is that electrostatic dust transport redistributes smaller, and hence brighter, dust particles in these regions (Garrick-Bethell et al. 2011).

As NASA is returning to the surface of the Moon for a long-term, sustainable presence, electrostatic dust charging and transport has been recognized to be one of the biggest challenges to overcome. Lunar dust is known to cause issues as learned from the Apollo missions (Afshar-Mohajer et al. 2015), including damage to spacesuits due to the abrasiveness of lunar dust (Godwin 2002); degradation of thermal radiators (Gaier et al. 2011a, 2011b), solar panels (Katzen et al. 1991) and retroreflectors (Murphy et al. 2010, 2014); and interference with extravehicular activity (EVA) systems (Gaier 2005). Lunar dust brought back to living quarters could lead to serious health risks when inhaled by astronauts (James & Khan-Mayberry 2009). Understanding lunar dust transport and its efficiency is vital to assessing its impact on crew safety and the operation of exploration systems.

Beyond the Moon, electrostatic dust transport has also been indicated on other airless bodies, including the dust ponds on asteroid 433 Eros (Robinson et al. 2001; Colwell et al. 2005),



Original content from this work may be used under the terms of the [Creative Commons Attribution 4.0 licence](#). Any further distribution of this work must maintain attribution to the author(s) and the title of the work, journal citation and DOI.

the spokes in Saturn's rings (Smith et al. 1981; Morfill et al. 1983), and the rocky surfaces of asteroids Benu and Ryugu (Jaumann et al. 2019; Lauretta et al. 2019) as a result of electrostatic dust escape (Hsu et al. 2022). Observing electrostatic dust transport on the Moon will advance our understanding of this process and its effect on the surface evolution of all airless bodies in the solar system.

Motivated by the existing observations and the needs recognized for future explorations, dust charging and lofting have been investigated in laboratory experiments under various plasma conditions (Sickafoose 2002; Flanagan & Goree 2006; Wang et al. 2009, 2010, 2011; Ding et al. 2013). Previous charging theories, including the shared charge model (Flanagan & Goree 2006) and charge fluctuation theory (Sheridan et al. 1992; Flanagan & Goree 2006; Sheridan & Hayes 2011), treated dust particles as part of the surface itself on a macroscale. However, these models could not explain the dust lofting demonstrated in the laboratory and possible lofting indicated by the space observations. Recently, a microscale patched charge model (PCM) advanced the fundamental understanding of the dust-charging and -lofting mechanism (Wang et al. 2016). The PCM shows that the emission and reabsorption of photoelectrons generated by UV radiation and/or secondary electrons due to the impact of energetic electrons or ions within microcavities between dust particles can result in the buildup of large negative charges on the surrounding particles. Subsequently, strong Coulomb repulsive forces between these negatively charged particles lead to their lofting. Simulations (Zimmerman et al. 2016; Deca et al. 2023) and follow-up experiments have verified the PCM and provided more insights into the dust lofting properties, including initial charge and velocity distributions (Schwan et al. 2017; Orger et al. 2019; Carroll et al. 2020), size distributions (Hood et al. 2022), lofting rates (Hood et al. 2018), as well as mobilization in the presence of magnetic fields (Yeo et al. 2022). These laboratory results provide critical constraints for designing in situ instrumentation and measurements.

To solve the long-standing fundamental problem of electrostatic dust charging and lofting on the lunar surface, the high-fidelity and flight-qualified prototype of an in situ dust instrument, the Electrostatic Dust Analyzer (EDA), has been developed and achieved Technology Readiness Level (TRL) 6 under NASA's Development and Advancement of Lunar Instrumentation (DALI) program. EDA will provide unambiguous, direct measurements of dust transport on the lunar surface. This paper describes the EDA instrument's design, development, and performance results.

## 2. Instrument Description

The EDA instrument consists of two modules: the sensor and the digital signal processing (DSP) modules. Depending on mission objectives and capabilities, EDA can be configured in different ways. For example, EDA can be accommodated in a lander, deployed from a lander to be close to or placed directly on the surface, or accommodated on a rover for mobility to survey a larger area. EDA is designed to measure dust transport anywhere on the lunar surface. Figure 1(a) shows a notional configuration. The sensor module is placed on the lunar surface, and the DSP module is mounted on a lander with a harness connecting the two modules to provide power and communication from the lander.

EDA measures the charge, velocity, mass (size), and flux of electrostatically lofted dust particles as they fall back onto the lunar surface. The measurement requirements and EDA performance are summarized in Table 1, showing the performance meets or exceeds the requirements. The measurement requirements are determined based on the Apollo observations and recent laboratory results as described in Section 1. The dust size requirement of 2–20  $\mu\text{m}$  in radii is determined based on the average size estimated from the LHG observations (Rennilson & Criswell 1974) and significant populations of lofted dust recorded in the laboratory experiments (Carroll et al. 2020; Hood et al. 2022). The observed height of the LHG (Rennilson & Criswell 1974) and laboratory measurements of initial velocities (Carroll et al. 2020) establish the velocity requirement of 1.25–10  $\text{m s}^{-1}$  for the defined size range. Based on the initial charge of lofted dust measured in the laboratory (Schwan et al. 2017) and accounting for its dynamic change through the near-surface plasma environment (Yeo et al. 2021), the charge magnitude is determined to be 2.4–24 fC for both positive and negative polarities. The dust flux is bounded using a transient flux of lofted dust  $\sim 0.5 \text{ cm}^{-2} \text{ s}^{-1}$  suggested from the LHG observations (Rennilson & Criswell 1974).

A tilt mechanism allows EDA to change its elevation angle  $\pm 90^\circ$  relative to the surface to measure particles with a range of trajectories. EDA has two reclosable doors, one on each end of the instrument. The anti-Sun door is opened to capture dust, while the opposing door remains closed to prevent the UV light and charged plasma particles from entering the instrument, minimizing spurious charge signals interfering with dust measurements. The tilt and door opening mechanisms utilize a lightly preloaded friction seal to keep dust out of their joints. A lander on the lunar surface will be charged, and it will disturb the surrounding plasma environment, subsequently affecting dust charging and lofting on the lunar surface. Figure 1(b) shows simulated potential profiles around a lander with typical solar wind and UV conditions at different incident angles. These simulations indicate that, in general, the sensor module should be at least 1 m away from the lander and stay outside its plasma wake to minimize the lander's influence on measurements of naturally lofted dust from the surface.

A cut view of the sensor module is shown in Figure 2(a), including the sensor, charge sensitive amplifiers (CSA), data acquisition (DAQ) board, power services board, and an accelerometer. A block diagram shows these key components and their functional relationships in both the sensor and DSP modules (Figure 2(b)). Figure 3 shows photographs of the high-fidelity and flight-qualified EDA sensor module (TRL 6). The mass of the EDA sensor module is 4.3 kg, and the power consumption is 5 W. The DSP module is not within the scope of the EDA prototype development; instead, its functions are implemented using a desktop computer.

### 2.1. Sensor Design

The EDA sensor module inherits its measurement techniques from the dust trajectory sensor (Auer 1975; Auer et al. 2008, 2010; Xie et al. 2011, 2013; Sternovsky et al. 2015) and the electrostatic lunar dust analyzer (Duncan et al. 2011) instruments. The sensor module consists of two identical dust trajectory sensor (DTS) units, one on each end of the instrument, and a deflection field electrode (DFE) unit lying in between (Figure 4). Two electron rejection grid (ERG) units

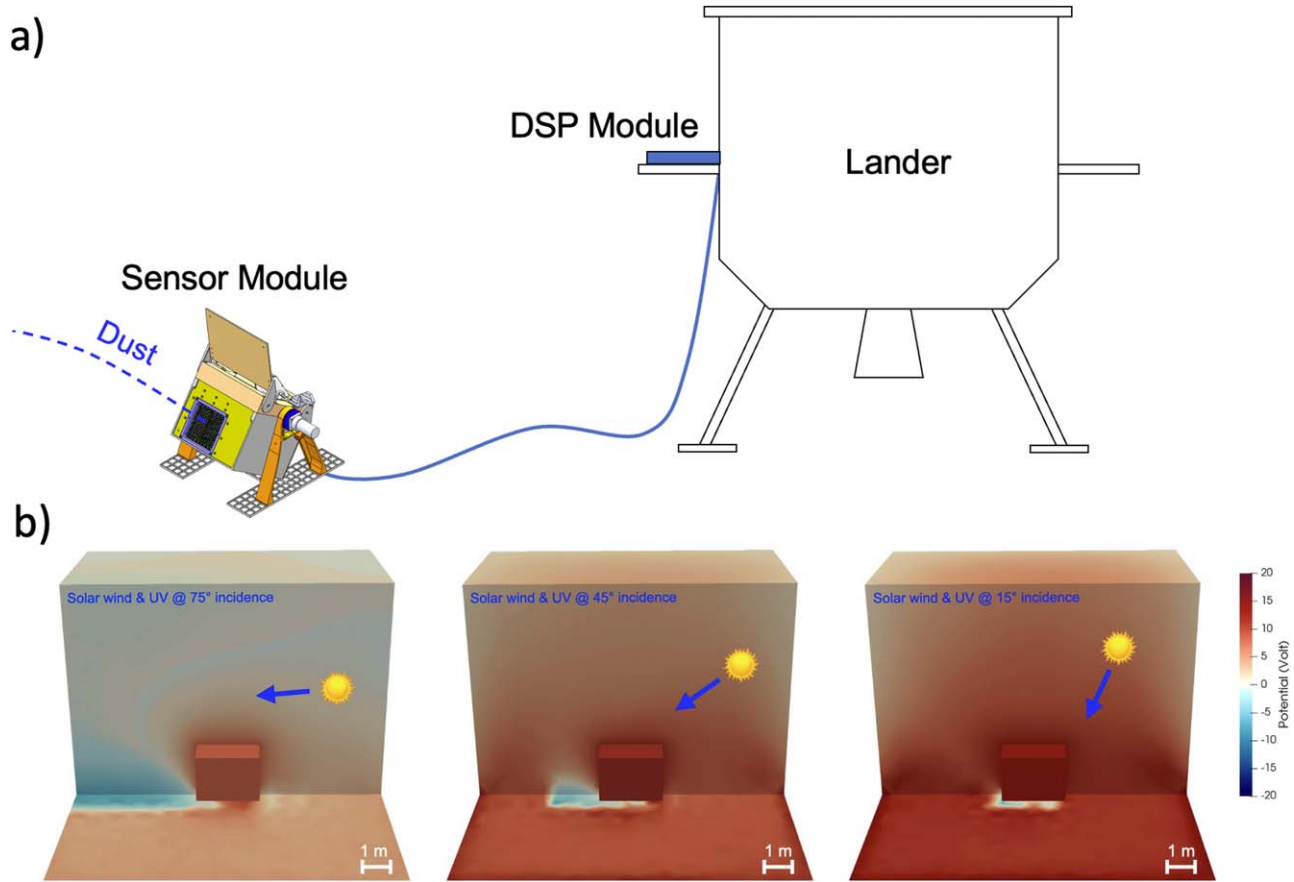


**Figure 1.** (a) A notional EDA configuration with a lander for dust transport measurements on the lunar surface. EDA collects lofted dust particles that fall back onto the surface. The EDA sensor module is placed on the surface and connected with the digital signal processing (DSP) module on the lander. (b) Simulations of the plasma environment around a lander (a 2 m cube in the center of the plots) with typical solar wind and UV conditions at different incident angles.

**Table 1**  
EDA Measurement Parameters

Parameter	Measurement Requirements	EDA Performance
Dust Size ( $\mu\text{m}$ )	$2 < r < 20$	$1 < r < 20$
Accuracy (%)	50	15
Dust velocity ( $\text{m s}^{-1}$ )	$1.25 < v < 10$	$0.8 < v < 20$
Accuracy (%)	50	15
Dust charge (fC)	$2.4 < Q < 24$	$1.2 < Q < 64$
Accuracy (%)	50	20
Polarity	positive/negative	positive/negative
Dust flux (particles $\text{cm}^{-2} \text{s}^{-1}$ )	$5 \times 10^{-5} < F < 0.5$	$0 < F < 1.7$
Accuracy (%)	50	20
Cadence (minute)	<1	continuous
FOV (deg)	...	54 (for size meas.)
FOV (deg)	...	135 (for flux meas.)

biased between 0 and  $-125 \text{ V}$  are located in the instrument entrances to reject ambient electrons at the lunar surface while allowing dust particles to enter the instrument without changing their trajectories. The ERG is nominally set to be  $-10 \text{ V}$  if the lunar photoelectrons dominate the noise floor or  $-50 \text{ V}$  if the solar wind electron contribution is significant.

Upon entering the instrument, a charged dust particle induces charges on two arrays of seven wire electrodes in the DTS (Figure 4). Each wire electrode is 8 cm long and 0.5 mm in diameter oriented along the y-axis. The dimensions of the wire electrodes are chosen for the highest sensitivity based on previous studies (Auer et al. 2008). The induced charge on each wire electrode is measured by an individual CSA. Examples of induced charge signals are shown in Figure 4 (upper left). The charge of the dust particle is measured as the sum of the magnitudes of induced charge signals on all the wire electrodes in the DTS as the particle passes through it. The magnitude is approximately inversely proportional to the distance between the particle and the wire electrode. The 2D trajectory of the particle is reconstructed from the recorded signals of all wire electrodes, which determines the particles velocity vector in the  $x$ - $z$ -plane.

The dust particle is deflected in the deflection field electrodes (DFE) region that consists of a set of two positively and one negatively biased electrode plates (Figure 4). A grounding grid is located on each side of the DFE to shield its influence on charge measurements in the DTS units. The charge-to-mass ratio,  $Q/m$ , is determined from the angle of deflection that scales approximately as  $\tan \delta = (El/v_x^2)(Q/m)$ , where  $E$  is the electric field between the electrodes with length  $l$  and  $v_x$  is the velocity component along the  $x$ -axis. Given the dust mass density ( $\sim 3 \text{ g cm}^{-3}$  for typical lunar dust; Mitchell et al. 1972), the particle size is calculated. The dust trajectory is analyzed with consideration of the DFE electric field and surface



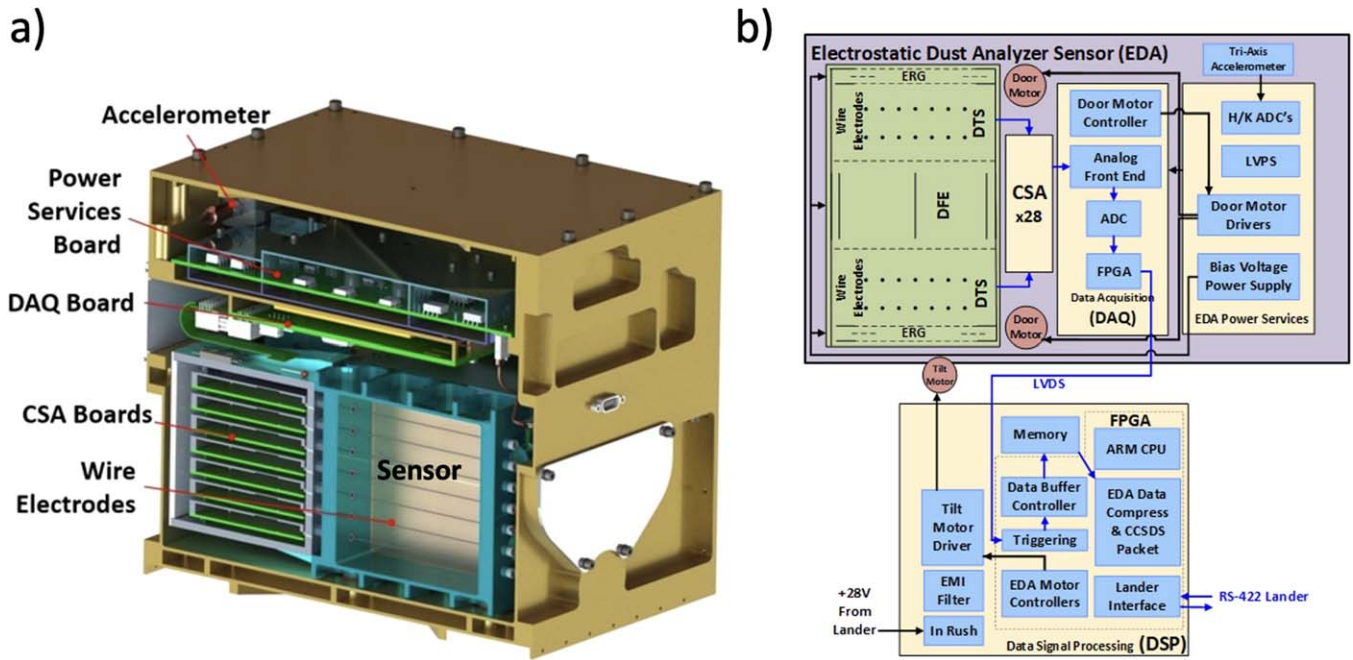


**Figure 2.** (a) Cut view of the EDA sensor module; (b) functional block diagram of the EDA sensor and DSP modules.

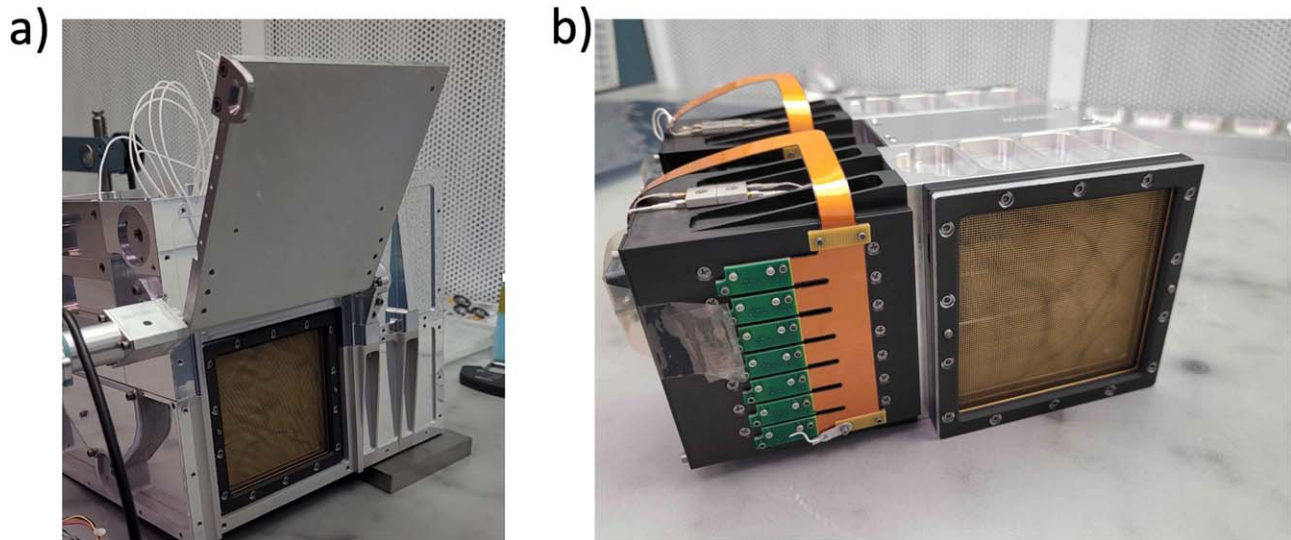


**Figure 3.** High-fidelity and flight-qualified prototype (TRL 6) of the EDA instrument. (a) The sensor module with an opening door; (b) the sensor core.

gravitational acceleration on the body of interest (Duncan et al. 2011; Xie et al. 2011, 2013).

The field of view (FOV) of the instrument is  $135^\circ$  for dust particles to be detected as they pass through the first wire-electrode array. To determine the mass (size), particles are required to pass through all four wire-electrode arrays, resulting in an FOV of  $54^\circ$ . The 2D velocity measured within this FOV is underestimated from the true velocity by  $<15\%$  due to the unknown velocity component in the y-axis.

## 2.2. Electrical Design

EDA employs a total of 28 CSAs, one for each wire electrode, measuring the induced charge from dust particles. The CSA is implemented in a two-stage design and the AC coupling in between eliminates any DC offsets from the first

stage (Figure 5). The 3.2 Hz–1 kHz bandwidth of the CSA is optimized for the velocity range of dust particles to be measured (Table 1). The noise of CSA sets the sensitivity of the instrument and is minimized by the selection of components and by implementing lessons learned from the development of previous laboratory prototype instruments (Duncan et al. 2011; Xie et al. 2011, 2013).

EDA is an event-driven and self-triggered instrument. The digitized signals from the 14 CSA channels in a DTS unit at the dust entrance are continuously fed into a field programmable gate array (FPGA) operated as a transient recorder. Simultaneously, the FPGA runs a set of optimal filters (Thomas et al. 2013) for each CSA channel. The simultaneous detection of signals on multiple channels provides a high-fidelity trigger signal upon which the DAQ is completed and transferred to

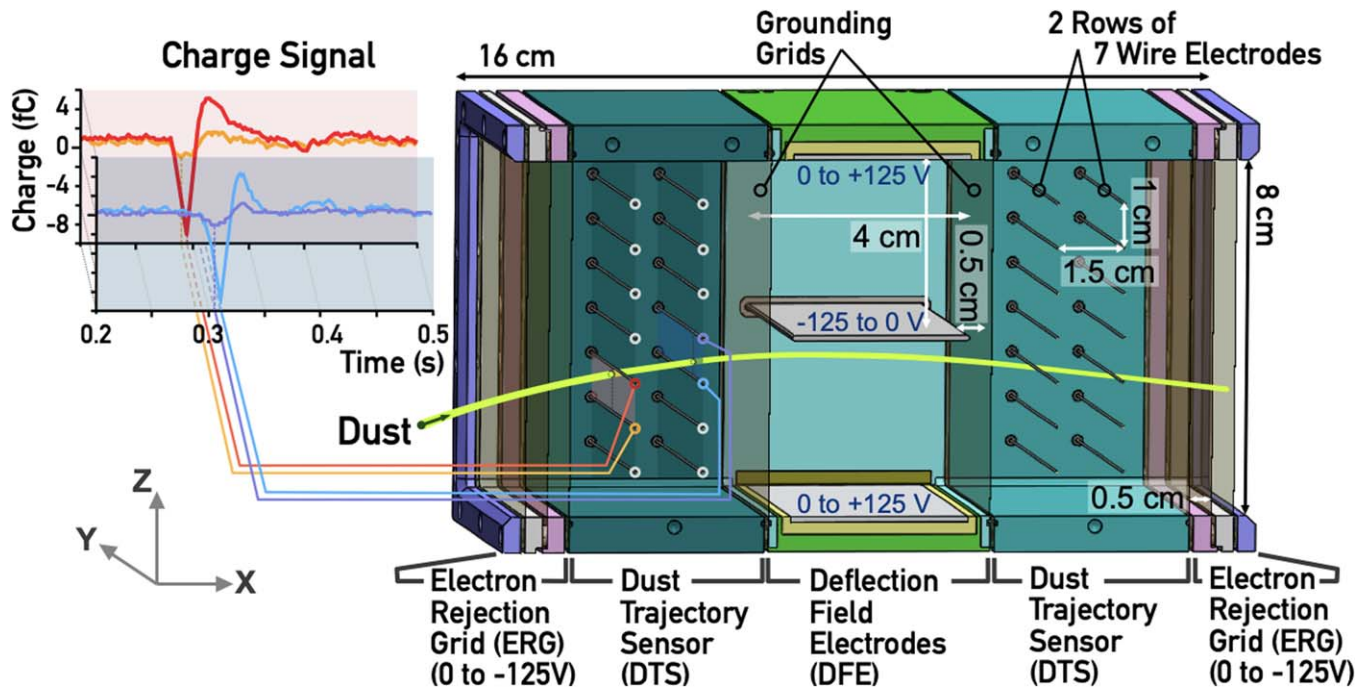


**Figure 4.** Cut view of the EDA sensor with the trajectory of a dust particle passing through the sensor. Examples of induced charge signals corresponding to the colored wire electrodes are shown in the upper left corner.

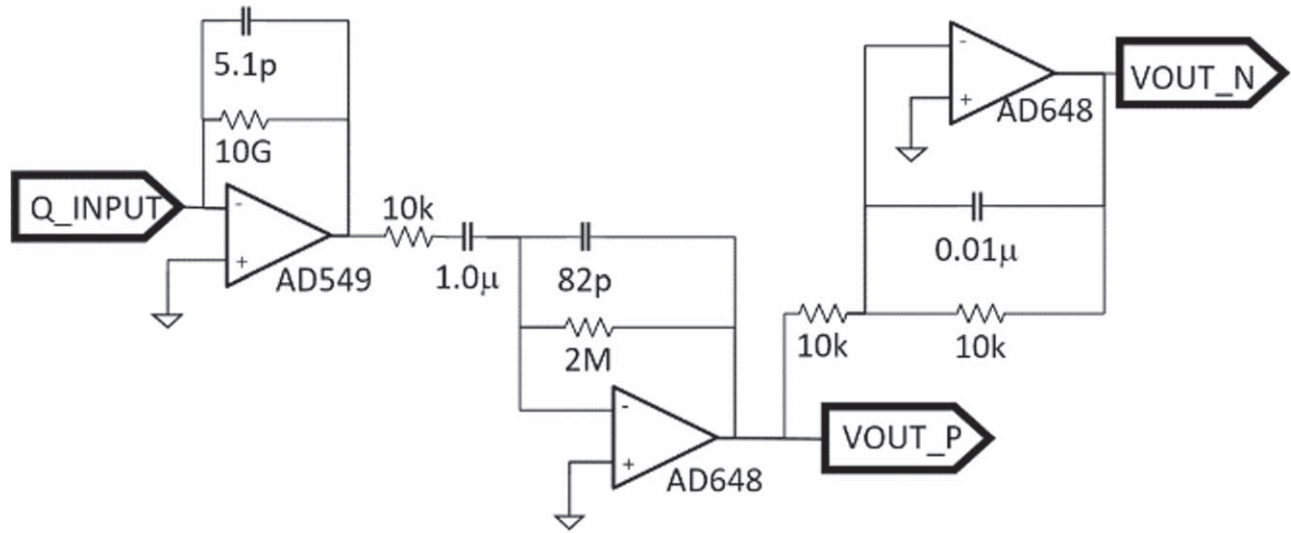


**Figure 5.** Schematic of the charge sensitive amplifier (CSA).

memory. The probability of self-triggering is  $>99\%$  for dust charge-to-noise ratio  $\geq 6.25$ , where the noise is expressed in rms charge equivalent (Auer et al. 2010).

### 3. Laboratory Testing and Results

#### 3.1. Dust Drop Test Setup

Dust drop tests were performed in a vacuum chamber with a pressure of  $7 \times 10^{-7}$  Torr (Figure 6(a)). JSC-1A lunar simulant particles (McKay et al. 1994) were loaded on a thin metal sheet with a small hole in the middle in a dust dropper. A solenoid was pulsed to shake the metal sheet to allow 1–2 particles to fall out of the hole at once. The falling particle carries charge due to the triboelectric effect. The particle fell through a pickup tube, 3 cm long and 0.5 cm in diameter, placed right below the

dust dropper. The charge measured by the pickup tube is used to verify EDA measurements. An example of the pickup tube measurements shows a pair of the entry and exit charge signals (Figure 6(b)). EDA was mounted on a two-axis translation stage and placed 20 cm below the dust dropper. Three experiments were performed: (1) drop of large particles ( $100\text{--}112\ \mu\text{m}$ ) without a DFE bias voltage; (2) drop of small particles ( $35\text{--}48\ \mu\text{m}$ ) without a DFE bias voltage; and (3) drop of small particles ( $35\text{--}48\ \mu\text{m}$ ) with a 1500 V DFE bias voltage. Experiments (1) and (2) examine detection of the dust charge over a wide range and the dust velocity, and experiment (3) determines the dust mass (size) derived from the deflected trajectory by DFE in addition to the charge and velocity. Note that, on the lunar surface, a  $\pm 125$  V bias on DFE is determined to be sufficient to cause detectable deflection for mass (size)

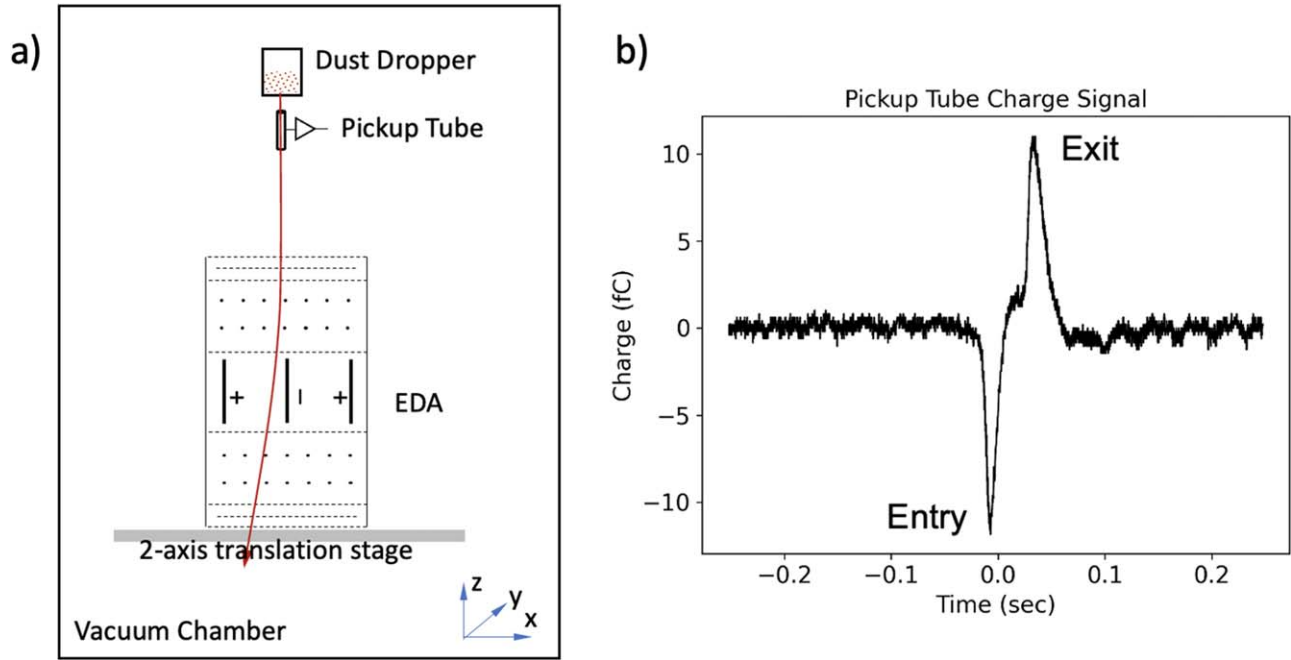


**Figure 6.** (a) Schematic of the dust drop setup in a vacuum chamber. (b) Example of pickup tube charge signals as a dust particle enters and exits the tube.

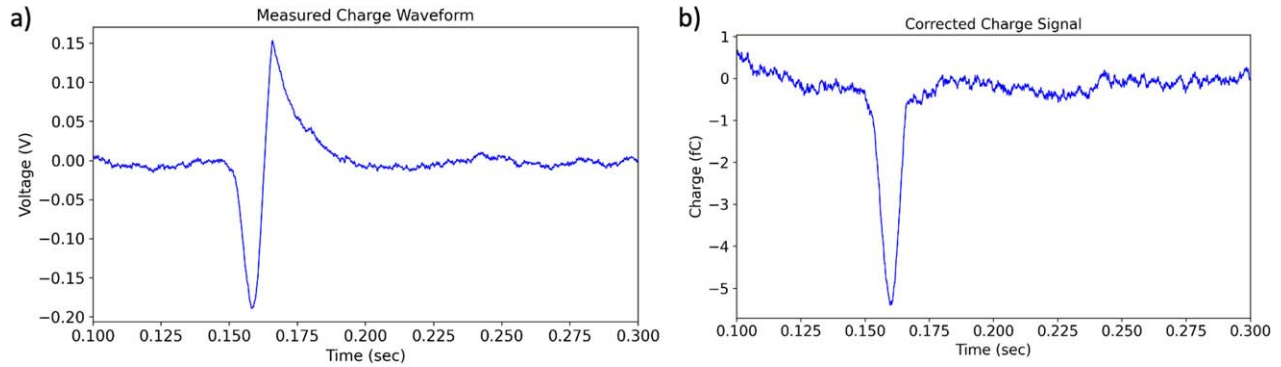


**Figure 7.** (a) Example of a measured charge waveform on a wire electrode and (b) corrected charge signal using the impulse response of the CSA circuit.

measurements based on the dust charge estimated for the lunar surface plasma environment (Yeo et al. 2021).

### 3.2. Data Analysis

The data analysis follows the following steps:

(1) Convert the analog-to-digital converter data of all 28 wire electrodes to charge waveforms (in voltage) as a function of time. An example waveform is shown in Figure 7(a).

(2) Convert and correct charge waveforms to charge signals. Figure 7(a) shows a charge overshoot due to the limited bandwidth. An impulse response of the CSA circuit was measured and used to retrieve true charge signals by applying a transfer function:  $x(t) = \text{FFT}^{-1}[\text{FFT}(Y(t))/\text{FFT}(h(t))]$ , where  $x(t)$  is the CSA input waveform,  $Y(t)$  is the measured output waveform, and  $h(t)$  is the CSA impulse response. A corrected charge signal is shown in Figure 7(b).

(3) Determine dust locations in all four wire-electrode arrays and the dust charge. Based on the ratios of the charge magnitudes of all seven wire electrodes in the same array, the dust location is determined, which is approximately inversely

proportional to the charge magnitude ratio. Examples are shown in Figures 8–10 in Section 3.3. To increase accuracy, a lookup table is created by modeling charge distributions on all the wire electrodes for a dust particle at various locations in the DTS using the commercial SIMION software (Dahl 2000). When the dust location is determined, the charge of the dust particle is the sum of the charge magnitudes measured on all 14 wire electrodes in the DTS with a compensation for the induced charge loss to the instrument wall.

(4) Reconstruct the dust trajectory passing through the instrument to determine the dust velocity. The trajectory is reconstructed from the four locations determined in the wire-electrode arrays. The 2D velocities in the  $x$ - $z$ -plane (Figure 4) in the two DTS units are thus determined. These velocities are up to 15% underestimated than the true velocities due to the unknown velocity component in the  $y$ -axis, as described in Section 2.1.

(5) Fit the dust trajectory to derive the dust mass (size). The dust mass is determined by fitting a dust trajectory to all four locations in the wire-electrode arrays with the determined charge and entry velocity. Given the dust mass density



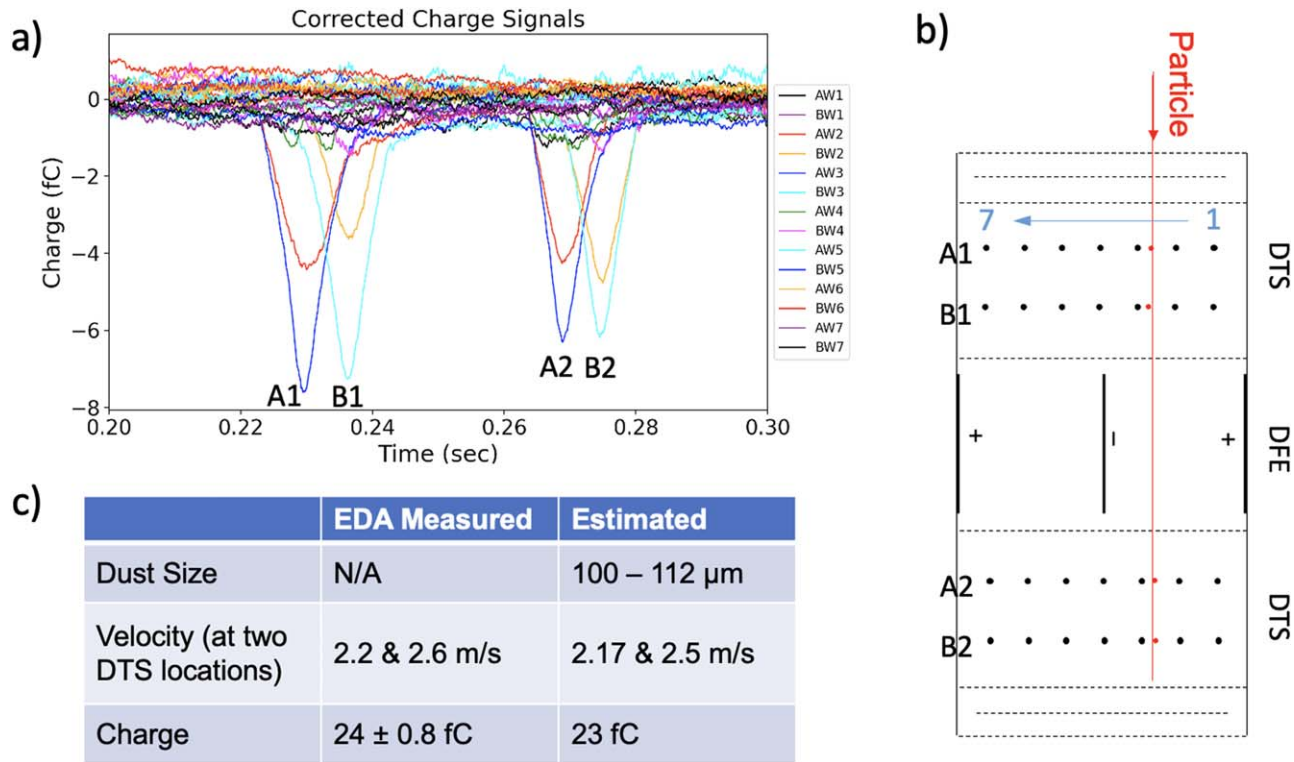


**Figure 8.** (a) Charge signals induced on all 28 wire electrodes as a 100–112  $\mu\text{m}$  dust particle passes through the EDA sensor without a DFE bias; (b) dust particle locations in four wire-electrode arrays are determined from charge signal ratios between the wire electrodes, showing a straight downward trajectory; and (c) dust characteristics measured by EDA in comparison to the estimated values.

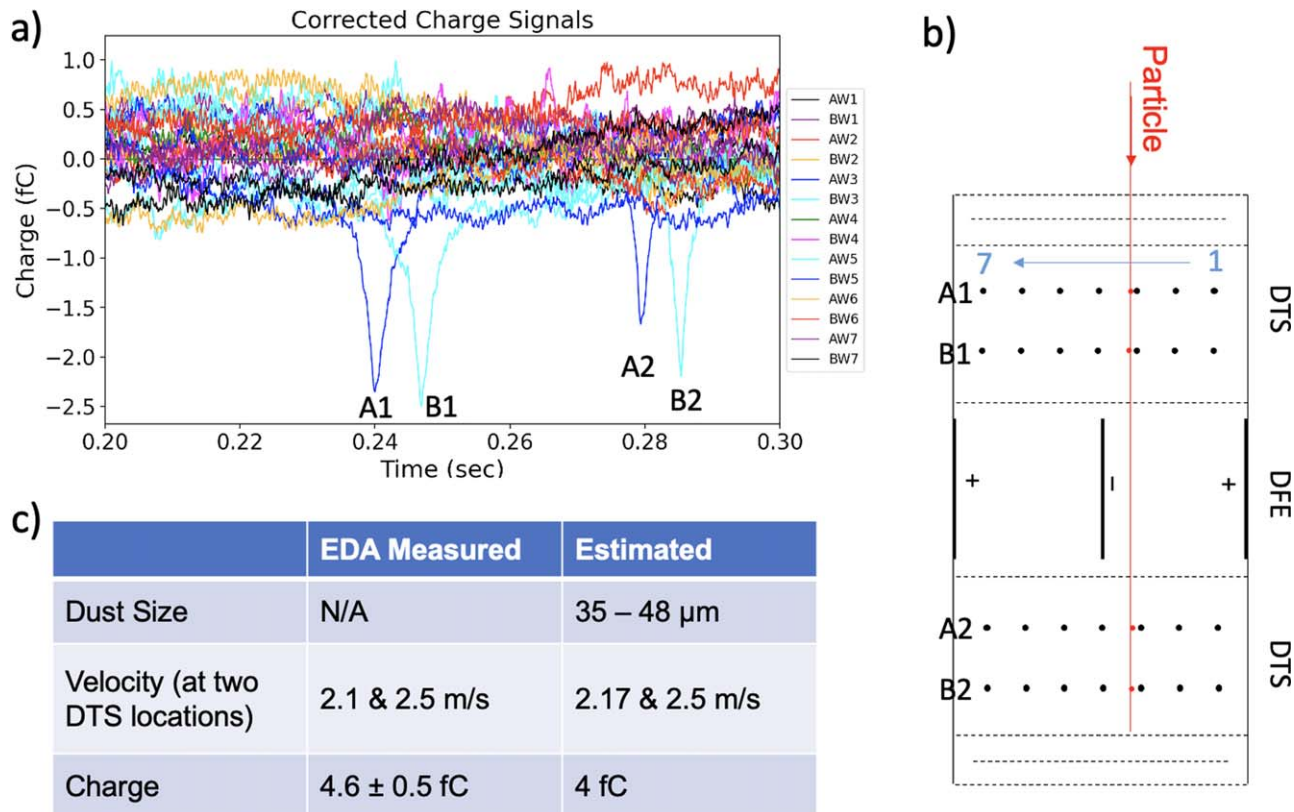


**Figure 9.** (a) Charge signals induced on all 28 wire electrodes as a 35–48  $\mu\text{m}$  dust particle passes through the EDA sensor without a DFE bias; (b) dust particle locations in four wire-electrode arrays are determined from charge signal ratios between the wire electrodes, showing a straight downward trajectory; and (c) dust characteristics measured by EDA in comparison to the estimated values.

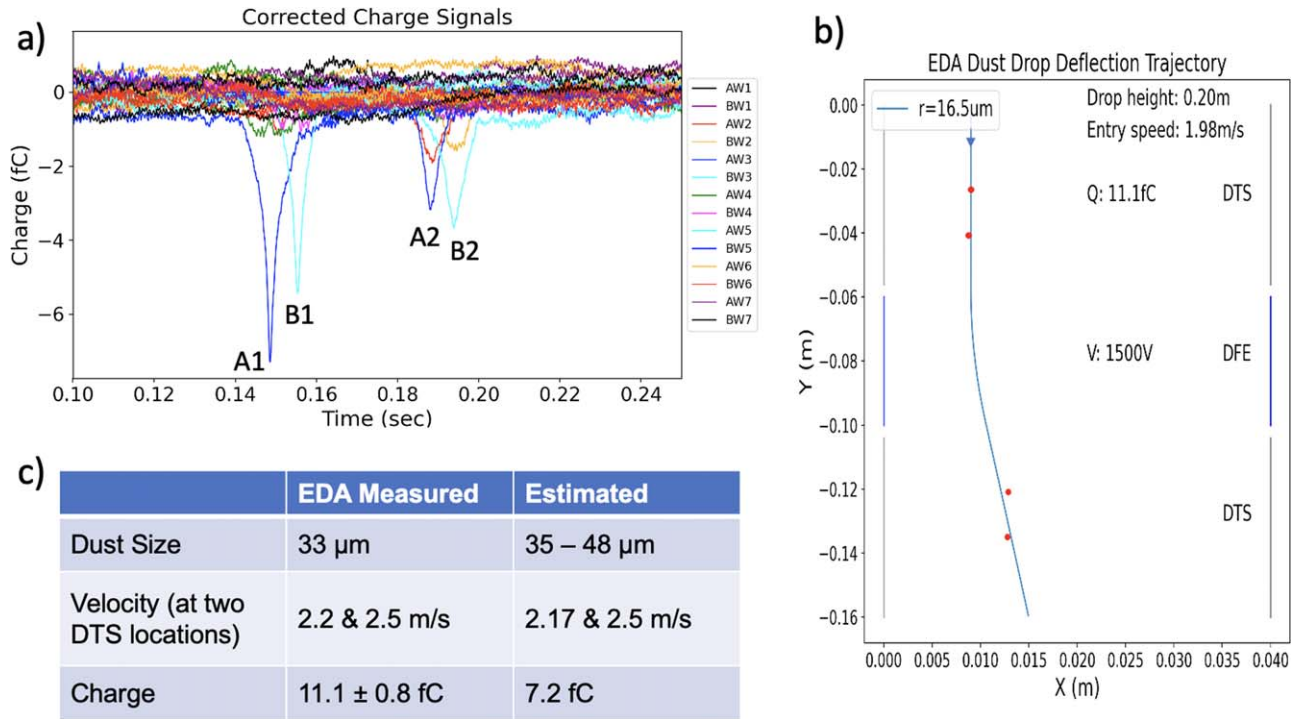


**Figure 10.** (a) Charge signals induced on all 28 wire electrodes as a 35–48  $\mu\text{m}$  dust particle passes through the EDA sensor with a DFE bias at 1500 V; (b) dust particle locations in four wire electrode arrays are determined from charge signal ratios between the wire electrodes. A deflection trajectory that best fits the particle locations determines the particle size; and (c) dust characteristics measured by EDA in comparison to the estimated values.

(2.9 g cm<sup>-3</sup> for JSC-1A used in the laboratory tests; McKay et al. 1994), the dust size is determined.

### 3.3. Results

Examples of the testing results in three experiments, as described in Section 3.1, are shown in Figures 8–10. These figures show corrected charge signals in (a), determined dust locations and trajectories in (b), and derived parameters including the dust charge, velocity, and size in (c) in comparison to the estimated values.

JSC-1A particles were sifted with sieves to constrain the dust size with narrow distributions. The estimated dust charge was measured using the pickup tube. Two velocities were measured in two DTS units, respectively. Due to gravity, the velocity in the exit DTS is slightly larger than that in the entry DTS. The estimated values are the free-fall velocities calculated for dust falling down from the dropper.

Figures 8 and 9 show results of large and small dust particles falling through the instrument without a DFE bias voltage. As shown in (b) of both figures, the dust trajectories are straight down without deflection. The dust size is thus not determined. Both velocity and charge measurements have good agreement with the estimated values (within 4% for the velocity and 15% for the charge measurements), as shown in (c) in both figures. In Figure 9(a), the dust charge as small as 4.6 fC is readily resolved with respect to the noise floor of 0.5 fC. All of these measured parameters exceed the performance requirements shown in Table 1.

Figure 10 shows a small dust particle falling through the instrument with a DFE bias voltage applied. A dust trajectory is determined using the determined charge and velocity with varying the dust size (mass) until it fits the measured dust locations, showing deflection of the trajectory by the DFE

(Figure 10(b)). The dust size is thus determined, showing good agreement with the lower limit of the size distribution (within 6%), which exceeds the performance requirements (Table 1). Again, the measured velocity shows high accuracy (within 2%). The charge measured by EDA is larger than the estimated value from the pickup tube measurement in this test. Overall, all the key parameters, including the charge, velocity, and size, show good accuracy that meets or exceeds the performance requirements of the EDA instrument.

## 4. Environmental Testing

EDA underwent environmental testing per GSFC-STD-7000 General Environmental Verification Standard (GEVS) to achieve TRL 6. Vibration (14.1 grms) and quasi-static (42 g) testing was performed in three axes to proto-flight levels with functional testing pre-/post-testing to verify EDA survived the launch loads. EDA then underwent thermal vacuum cycling to operational and survival temperatures based upon maximum worst-case predicted temperatures for an equatorial (hot) and polar (cold) landing area on the Moon. A total of one survival (–50°C to +85°C) cycle and four operational cycles (–35°C to +80°C) were performed with functional tests at each temperature plateau to verify EDA performed nominally over the full temperature range.

## 5. Conclusion

A high-fidelity and flight-qualified EDA instrument has been developed to measure the charge, velocity, mass (size), and flux of electrostatically lofted dust on the lunar surface. EDA consists of two dust trajectory sensor (DTS) units on both ends of the instrument and a DFE unit lying in between. Upon entering the instrument, a charged dust particle induces charges on the arrays of the wire electrodes in the DTS units, which



determine the total charge of the dust particle. Based on the charge magnitude ratios between the wire electrodes, the dust particle's locations are determined to reconstruct its trajectory passing through the instrument from which the dust velocity and mass (size) are derived. A dust campaign was performed in a vacuum chamber to characterize the performance of the instrument. The results show that all the key parameters, including the dust charge, velocity, and size, meet or exceed the performance requirements. EDA passed both vibration and thermal cycling environmental tests and has achieved TRL 6. EDA measurements on the lunar surface are expected to solve a more than five-decade-old problem about electrostatic dust charging and lofting and play a critical role in assessing the dust environment on the lunar surface and its impact on human and robotic exploration. Additionally, EDA measurements will have important implications for the surface evolution of airless bodies, including the Moon and asteroids, in the solar system.

### Acknowledgments

This work was supported by the NASA Development and Advancement of Lunar Instrumentation (DALI) program (grant No. 80NSSC19K0765).

### ORCID iDs

X. Wang  <https://orcid.org/0000-0001-8472-7079>

### References

- Afshar-Mohajer, N., Wu, C.-Y., Curtis, J. S., & Gaier, J. R. 2015, *AdSpR*, **56**, 1222
- Auer, S. 1975, *RSci*, **46**, 127
- Auer, S., Grün, E., Kempf, S., et al. 2008, *RSci*, **79**, 084501
- Auer, S., Lawrence, G., Grün, E., et al. 2010, *NIMPA*, **622**, 74
- Berg, O. E., Wolf, H., & Rhee, J. 1976, in *Interplanetary Dust and Zodiacal Light*, Lecture Notes in Physics, Vol. 48, ed. H. Elsaesser & H. Fechtig (Berlin: Springer), 233
- Blewett, D. T., Coman, E. I., Hawke, B. R., et al. 2011, *JGRE*, **116**, E02002
- Carroll, A., Hood, N., Mike, R., et al. 2020, *Icar*, **352**, 113972
- Colwell, J. E., Gulbis, A. A. S., Horányi, M., & Robertson, S. 2005, *Icar*, **175**, 159
- Criswell, D. 1973, in *Proc. of the 6th ESLAB Symp., Photon and Particle Interactions with Surfaces in Space, Astrophysics and Space Science Library*, Vol. 37, ed. R. J. L. Garra (Dordrecht: Reidel), 545
- Dahl, D. A. 2000, *IJMSp*, **200**, 3
- Deca, J., Hsu, H.-W., Wang, X., & Horányi, M. 2023, AGUFM, P23B-03
- Ding, N., Wang, J., & Polansky, J. 2013, *ITPS*, **41**, 3498
- Duncan, N., Sternovsky, Z., Grün, E., et al. 2011, *P&SS*, **59**, 1446
- Feldman, P. D., Glenar, D. A., Stubbs, T. J., et al. 2014, *Icar*, **233**, 106
- Flanagan, T. M., & Goree, J. 2006, *PhPl*, **13**, 123504
- Gaier, J. R. 2005, The Effects of Lunar Dust on EVA Systems During the Apollo Missions NASA/TM-2005-213610, NASA, <https://ntrs.nasa.gov/api/citations/20050160460/downloads/20050160460.pdf>
- Gaier, J. R., Journey, K., Christopher, S., & Davis, S. 2011a, Evaluation of Brushing as a Lunar Dust Mitigation Strategy for Thermal Control Surfaces NASA/TM-2011-217231/ AIAA-2011-5182, NASA, <https://ntrs.nasa.gov/api/citations/20120000070/downloads/20120000070.pdf>
- Gaier, J. R., Waters, D. L., Misconin, R. M., Banks, B. A., & Crowder, M. 2011b, Evaluation of Surface Modification as a Lunar Dust Mitigation Strategy for Thermal Control Surfaces NASA/TM-2011-217230/AIAA-2011-5183, NASA, <https://ntrs.nasa.gov/api/citations/20120000064/downloads/20120000064.pdf>
- Garrick-Bethell, I., Head, J. W., III, & Pieters, C. M. 2011, *Icar*, **212**, 480
- Glenar, D. A., Stubbs, T. J., Hahn, J. M., & Wang, Y. 2014, *JGRE*, **119**, 2548
- Glenar, D. A., Stubbs, T. J., McCoy, J. E., & Vondrak, R. R. 2011, *P&SS*, **59**, 1695
- Godwin, R. 2002, Apollo 17 : the NASA Mission Report (Burlington, Ontario: Apogee Books)
- Grün, E., & Horányi, M. 2013, *P&SS*, **89**, 2
- Hood, N., Carroll, A., Mike, R., et al. 2018, *GeoRL*, **45**, 13206
- Hood, N., Carroll, A., Wang, X., & Horányi, M. 2022, *Icar*, **371**, 114684
- Hsu, H.-W., Wang, X., Carroll, A., Hood, N., & Horányi, M. 2022, *NatAs*, **6**, 1043
- James, J. T., & Khan-Mayberry, N. 2009, The Human Research Program Evidence Book, NASA-SP-2009-3045, <https://humanresearchroadmap.nasa.gov/evidence/reports/lunar%20dust.pdf>
- Jaumann, R., Schmitz, N., Ho, T. M., et al. 2019, *Sci*, **365**, 817
- Katzan, C. M., Brinker, D. J., & Kress, R. 1991, Space Photovoltaic Research and Technology Conf., NASA Lewis Research Center
- Lauretta, D. S., Dellagiustina, D. N., Bennett, C. A., et al. 2019, *Natur*, **568**, 55
- McCoy, J. E. 1976, LPSC, **1**, 1087
- McCoy, J. E., & Criswell, D. R. 1974, LPSC, **3**, 2991
- McKay, D. S., Carter, J. L., Boles, W. W., Allen, C. C., & Allton, J. H. 1994, Engineering, Construction, and Operations in Space IV (Reston, VA: ASCE), 857
- Mitchell, J. K., Houston, W. N., Scott, R. F., et al. 1972, LPSC, **3**, 3235
- Morfill, G., Grün, E., Goertz, C., & Johnson, T. 1983, *Icar*, **53**, 230
- Murphy, T. W., Adelberger, E. G., Battat, J. B. R., et al. 2010, *Icar*, **208**, 31
- Murphy, T. W., McMillan, R. J., Johnson, N. H., & Goodrow, S. D. 2014, *Icar*, **231**, 183
- Orger, N. C., Toyoda, K., Masui, H., & Cho, M. 2019, *AdSpR*, **63**, 3270
- Rennilson, J., & Criswell, D. R. 1974, *The Moon*, **10**, 121
- Robinson, M. S., Thomas, P. C., Veverka, J., Murchie, S., & Carcich, B. 2001, *Natur*, **413**, 396
- Schwan, J., Wang, X., Hsu, H.-W., Grün, E., & Horányi, M. 2017, *GeoRL*, **44**, 3059
- Sheridan, T. E., Goree, J., Chiu, Y. T., Rairden, R. L., & Kiessling, J. A. 1992, *JGR*, **97**, 2935
- Sheridan, T. E., & Hayes, A. 2011, *ApPhL*, **98**, 091501
- Sickafoose, A. A. 2002, *JGRA*, **107**, 1408
- Smith, B. A., Soderblom, L., Beebe, R., et al. 1981, *Sci*, **212**, 163
- Sternovsky, Z., Gemer, A. J., Grün, E., et al. 2015, in 2015 IEEE Aerospace Conf. (Piscataway, NJ: IEEE), 1
- Szalay, J. R., & Horányi, M. 2015, *GeoRL*, **42**, 5141
- Thomas, E., Auer, S., Drake, K., et al. 2013, *P&SS*, **89**, 71
- Wang, X., Horányi, M., & Robertson, S. 2009, *JGRA*, **114**, A05103
- Wang, X., Horányi, M., & Robertson, S. 2010, *JGRA*, **115**, A11102
- Wang, X., Horányi, M., & Robertson, S. 2011, *P&SS*, **59**, 1791
- Wang, X., Schwan, J., Hsu, H.-W., Grün, E., & Horányi, M. 2016, *GeoRL*, **43**, 6103
- Xie, J., Sternovsky, Z., Auer, S., et al. 2013, *P&SS*, **89**, 63
- Xie, J., Sternovsky, Z., Grün, E., et al. 2011, *RSci*, **82**, 105104
- Yan, Q., Zhang, X., Xie, L., et al. 2019, *GeoRL*, **46**, 9405
- Yeo, L. H., Hood, N., Wang, X., & Horányi, M. 2022, *PhRvE*, **106**, L013203
- Yeo, L. H., Wang, X., Deca, J., Hsu, H.-W., & Horányi, M. 2021, *Icar*, **366**, 114519
- Zimmerman, M., Farrell, W., Hartzell, C., et al. 2016, *JGRE*, **121**, 2150
- Zook, H. A., & McCoy, J. E. 1991, *GeoRL*, **18**, 2117